A Photonic Crystal Laser from Solution Based Organo-Lead Iodide Perovskite Thin Films

Songtao Chen[1], Kwangdong Roh[2], Joonhee Lee[1], Wee Kiang Chong[3], Emre Sari[1], Yao Lu[4], Nripan Mathews[5], Tze Chien Sum[3], Arto Nurmikko[1,2*]

[1]School of Engineering, Brown University, Providence, RI, 02912, USA

[2]Department of Physics, Brown University, Providence, RI, 02912, USA

[3]School of Physics & Mathematical Sciences, Nanyang Technological University, Singapore 637371, Singapore

[4]Department of Chemistry, Brown University, Providence, RI, 02912, USA

[5]School of Materials Science and Engineering, Nanyang Technological University, Singapore 639798, Singapore

Tel: +1 (401) 863-2869; Fax: +1 (401) 863-1387; Email: Arto_Nurmikko@brown.edu

Abstract

Perovskite semiconductors are actively investigated for high performance solar cells. Their large optical absorption coefficient and facile solution-based low temperature synthesis of thin films make perovskites also a candidate for light-emitting devices across the visible and near infrared. Specific to their potential as optical gain medium for lasers, early work has demonstrated amplified spontaneous emission and lasing at attractively low thresholds of photoexcitation. Here take an important step towards practically usable perovskite lasers where a solution-processed thin film is embedded within a two dimensional photonic crystal resonator. We demonstrate high degree of temporally and spatially coherent lasing whereby well-defined directional emission is achieved near 788 nm wavelength at optical pumping energy density threshold of 68.5 ± 3.0 μJ/cm^2.The measured power conversion efficiency and differential quantum efficiency of the perovskite photonic crystal laser is 13.8% and 35.8%, respectively. Importantly, our approach enables scalability of the thin film lasers to two-dimensional multielement pixelated arrays of microlasers which we demonstrate as proof-of-concept for possible projection display applications.

Organo-lead halide perovskites ($CH_3NH_3PbX_3$, where X=Cl, Br, I) have emerged as a new class of photovoltaic material candidates with reported high conversion efficiencies.[1] Their low-temperature solution-based synthesis makes perovskites attractive as candidate material for low-cost solar cells. Recently, light emission from perovskite thin films has also been studied including the exploration of possible optical gain. Attractively low threshold amplified spontaneous emission (ASE) was reported in solution-based polycrystalline films, under ultrashort (fsec) optical pumping.[2] Furthermore, single microcrystal perovskite optically pumped lasers with nanowire, nanodisk and nanoplatelet structure were fabricated by chemical vapor deposition or solution growth method.[3-6]. Elsewhere, stimulated emission from perovskites was demonstrated in form of random laser,[7] whispering-gallery mode laser using perovskite coated SiO_2 microsphere,[8] and vertical cavity configuration based on multilayer dielectric and gold reflectors.[9-10] Typically in these reports spectral narrowing and nonlinear threshold-like light input-output characteristics were presented as evidence for stimulated emission, yet none of these accomplishments have demonstrated efficient light extraction from their devices to emit well-defined, spatially-coherent beams – both a fundamental validation and a practical requirement for any laser claim. Here, we make a leap forward in both assessing and advancing the promise of a perovskite semiconductor laser by: (a) optimizing the microstructure of solution-based synthesis of high quality $CH_3NH_3PbI_3$ densely packed films to enable their conformal deposition on non-planar nanostructured substrates; (b) conformally integrating such perovskite films within two dimensional (2D) photonic crystal (PhC) nanostructure resonators to achieve spatially and temporally coherent optically pumped laser operation at high differential quantum efficiency, and (c) demonstrating the scalability of the PhC microlaser approach by implementing pixelated, individually addressable multielement laser arrays.

As optical resonators for microscale light emitters, photonic crystals are well-known optical nanostructures which have been deployed for high-end single crystal epitaxial III-V semiconductor diode lasers .[11-14] The basic version is a 2D-PhC with perfect hexagonal lattice structure which provides in-plane distributed optical feedback while in principle capable of further enhancing light-matter interaction.

The lattice-periodic change in the refractive index creates a photonic band structure, which in a laser device design is exploited by matching the band edge of the photonic crystal to the gain spectrum of the active medium for maximal Bragg reflections.[15-18] For the thin films of solution-grown polycrystalline perovskite, we designed the geometric parameters following the measurements of the film optical constants to spectrally match our particular $CH_3NH_3PbI_3$ films. The high refractive index ($n \sim 2.7$) of perovskite compared to quartz substrate ($n \sim 1.5$) increases the resonator mode spacing at the high symmetry Γ-points of the PhC, thereby offering a further benefit of single mode lasing operation.

Optical and electronic material quality is essential in pursuing meaningful laser devices. For solution-grown perovskite thin films a particular morphological challenge is to achieve sub-wavelength surface roughness in pinhole-free, densely packed solid films. Optimizing material synthesis for tight control of the grain size of the polycrystalline perovskite on the nanoscale is especially important here, for conformally wrapping the films across nano-pillar PhC structures without formation of voids and film discontinuities. Perovskite thin film synthesis is commonly realized in a one-step process, where the perovskite precursors are dissolved in a host solvent such as γ-butyrolactone (GBL), N,N-dimethylformamide (DMF), Dimethyl-sulfoxide (DMSO), etc. The solution is spin-cast onto the substrate, followed by thermal annealing to evaporate solvent residue and facilitate the crystallization process.[19-22] To further improve morphological quality of perovskite film, researchers have introduced methods, such as additive enhanced crystallization,[23] vacuum deposition,[24-26] use of a non-halide lead source,[27] or solvent-solvent extraction.[28]

In the one-step approach, rapid injection (“dripping”) of an extraction solvent onto the spinning sample was reported to aid in the formation of pinhole-free perovskite films.[21-22] The added extraction solvent (such as toluene) is miscible with the host solvent yet barely dissolves the perovskite. Work has been done on utilizing the combination of DMF and toluene as the host and extraction solvent controlled by carefully timed, rapid crystallization.[21] The drawback of this crystallization process during spin-casting is that small nucleates may not distribute uniformly because of the chaotic nature of high speed spin-

casting, resulting in non-uniform grain sizes distributed across a wide range (Supplementary Fig. S1). It has been shown that DMSO possesses a stronger Pb-O bond and coordination ability with lead iodide than DMF.[29] Making use of this property, crystallization of lead iodide can be retarded in the process of forming lead iodide film in a two-step method.[29-30] In this work, we hybridized these approaches in the literature by a custom process using DMSO as host solvent with a precisely controlled toluene dripping protocol. Consequently, we achieved optimized synthesis of a uniform distribution of tiny perovskite nucleates, followed by thermal annealing to complete the crystal growth (see Supplementary information; Figs. S2–S4).

Figure 1 summarizes the outcome of our synthesis-optimized perovskite thin films developed for optical nanostructures, first prepared on planar quartz substrates for characterization. Microstructure analysis shows closely packing of crystalline grains throughout the film (plan view in Fig. 1a and cross-sectional view in Fig. 1f). The root mean square (RMS) surface roughness is 11.3 nm (~ $\lambda/25$), extracted from AFM measurements (Fig. 1b). The grain size ranges from 30 ~ 120 nm which was judged to be sufficiently small for conformal incorporation into the non-planar photonic crystals templates. Photographs in Fig. 1c and Fig. 1d were taken immediately after the spin-casting and thermal annealing process, respectively, to qualitatively illustrate the optical transparency of the film. As noted, the crystallization process is driven to completion during thermal annealing whereby the pinkish color of as-spin-cast films changes to more darkish brown. Figure 1g shows two distinct absorption edges at 760 nm and 480 nm which have been identified as the principal inter-band electronic transitions in the perovskite thin films.[31] Room temperature photoluminescence (PL) of our perovskite films locates at 766.8 nm with a full width half maximum (FWHM) of 50.1 nm (105.8 meV). The relatively large PL linewidth (e.g. in comparison with solution grown CdSe quantum dots) reflects most likely the nanograin polydispersity which adds to inhomogeneous broadening in the multiparticle ensembles. We also estimated the (room temperature) quantum efficiency (QE) of our perovskite films by comparing their PL yield with commercial red CdSe/ZnS/CdZnS colloidal quantum dots (QD) with known QE ($\eta \geq 90\%$) from QD

Vision Inc. under low photoexcitation, obtaining an estimated value of $\eta \sim 20\%$. Such a relatively low QE value is likely due to non-radiative trap states on the non-passivated surface of perovskite grains. As shown below, however, at higher levels of photoexcitation, the moderate value of QE did not prevent achieving robust stimulated emission. It has also been reported that filling the trap states at higher pump levels, quantum yields from perovskites can be increased up to near unity[5,9].

In Fig. 2a, we show the refractive index and extinction coefficient spectra of perovskite film from spectroscopic ellipsometry to wavelengths well above the electronic resonances. The measured refractive index of $n = 2.6 \sim 2.7$ in the light emission range of 760 ~ 790 nm has a contribution from the high packing density, consistent with a published theoretical model.[32] The extinction coefficient shows near-zero value around 760 ~ 820 nm reaching a minimum at 784.9 nm. Although measuring small absolute values of the extinction coefficient accurately in perovskite films can be ambiguous in an ellipsometric measurement, we used the spectral shape as clue in identification of the spectral window for possible optical gain and to guide the design of the PhC structure. Informed by the values of the measured optical constants of the planar, dense perovskite thin films, we used the plane wave expansion (PWE) method for calculation of the PhC dispersion curves as shown in Fig. 2c (inset defines direction and critical points in reciprocal space). At the Γ-points there are four non-trivial frequencies which the PhC structure can support (region in the red dash circle is enlarged Fig. 2d). By variationally adjusting the relationship for periodic pitch (a) and pillar radius to pitch ratio (r/a), we optimized the spectral overlap at the Γ-points with the putative optical gain region of our perovskite films. We then fabricated two-dimensional hexagonal array PhC templates with 430 nm, 440 nm, 450 nm and 460 nm pitch, respectively. Electron beam lithography and reactive ion etching techniques were applied to pattern quartz substrates (fabrication summarized in supplementary Fig. S5). A scanning electron microscope (SEM) image of one particular PhC pattern (a = 450 nm) etched in quartz is shown in Fig. 2b. The average height of the pillars was measured to be 80.8 ± 4.9 nm. The next and most critical step was to deposit the perovskite films conformally and contiguously on the PhC templates. After optimizing the synthesis process as described

above, we succeeded in continuous and conformal deposition of the perovskite films on the nanopatterned substrate resulting in an optically smooth planar top surface as shown in the inset of Fig. 2b. The thickness of the perovskite film on the planar region of sample was 128.7 ± 2.6 nm.

With this synergistic materials and device approach to create the perovskite PhC (PePhC) hybrid device, we have succeed in achieving low threshold, single mode, spatially coherent laser operation in the near infrared region. We note that in contrast to the most commonly used femtosecond ultrashort pulse conditions in the literature, we deployed a more pragmatic, compact solid state laser as the excitation source, emitting 1000-fold longer sub-nanosecond pulsed (τ_{pulse} ~ 270 ps) in the green at λ = 532 nm with 1 kHz repetition rate. It is important to note that increasing the pump pulse duration adds to the requisite material quality as significant thermal stress is now imposed in each pulsed event. The pump beam was focused to a spot approximately filling a PhC target aperture (spot size: r ≈ 30 μm) in surface normal direction and the emission collected into a spectrometer through a long pass filter, likewise normal to the PePhC device plane.

Figure 3 summarizes the key findings of the new perovskite PePhC laser, displaying abrupt lasing threshold and excellent temporal and spatial coherence. The sharp lasing threshold and linewidth narrowing shown in Fig. 3a resembles that of a high performance III-V epitaxially grown semiconductor laser (inset emphasizes the spontaneous-to-stimulated emission threshold by plotting output on logarithmic scale). The measured pump energy density at threshold of 68.5 ± 3.0 μJ/cm^2 represents a most satisfactory outcome for a solution grown polycrystalline perovskite laser, especially given the well-defined spatially coherent output which we have achieved. At threshold, the low-level spontaneous emission transforms to stimulated emission with a measured differential (slope) quantum efficiency of 35.8%. Figure 3b highlights the single cavity mode lasing at λ = 788.1 nm, acquired from a PhC pattern with periodicity a = 450 nm at various excitation levels above threshold. Below threshold, the PePhC spontaneous emission has a broad spectrum with a Gaussian lineshape and linewidth $\Delta\lambda$ = 32.2 nm, which is narrowed from the planar perovskite film (FWHM $\Delta\lambda$ = 50.1 nm) and perhaps due to spectral filtering

by photonic crystal cavity.[33] Above threshold, the single mode linewidth collapses down to $\Delta\lambda = 0.24$ nm, which is near the resolution limit of our spectrometer (≥ 0.125 nm). Further insight to optical gain and lasing dynamics in the PePhC microlaser was obtained from emission rates measured directly by time domain techniques using the psec pulsed excitation source and fast avalanche photodiode. Near, yet below the threshold, the spontaneous emission lifetime remained in the nanosecond regime ($\tau_{sp} = 5.44 \pm 0.06$ ns; blue dots in Fig 3c). In the lasing regime, the corresponding decay time shortened abruptly to $\tau_{lasing} = 112.8 \pm 9.8$ ps at $P_{pump} = 1.1P_{th}$ (red dots in Fig 3c). The pronounced, nearly fifty-fold shortening of the emission lifetime reflects a corresponding acceleration in the stimulated emission rate in a transient, gain switching lasing regime. The time domain measurements showed further how the stimulated emission rate increased at higher excitation (supplementary figure S6). We note that while these results cannot be directly compared e.g. with the Schawlow-Townes model of (continuous wave) laser linewidth, the observed trend is empirically consistent with laser performance in a regime of good temporal coherence (monocromaticity) reflecting the synergy of robust optical gain in the perovskite films with the photonic crystal resonator.

Beyond temporal coherence, spatial coherence is fundamental to any laser with a useable output. We have achieved and characterized the well-defined output beams which emerge abruptly from the PePhC devices as the lasing threshold is crossed. The photographic images in the inset of Fig 3b shows the contrast between the diffuse luminescence below, and crisp laser beam emitted perpendicular to device plane above threshold. We quantified the transverse optical intensity distribution in a number of devices in the far field. Two types of far field beam patterns (transverse spatial modes) were generally observed (Fig. 3d, e), their relative contribution depending on the specific PhC template and level of photoexcitation, each mode (beam) displaying small angular divergence ($< 2°$). The pattern shown in Fig. 3d was typically found to be dominant, showing that it was possible to access one PhC Γ-point eigenmode in our hybrid PePhC laser. Small (nanometer scale) deviation from the geometrically ideal PhC structure due to limited resolution in the electron beam lithography process can in practice break the degeneracy to

enable single mode operation. For slightly different PhC patterns, lasing at different Γ-points can be activated as long as an overlap of the gain spectrum at the Γ-point photon energy is sufficient for net gain (Fig. 4a and remarks below). Additionally, we analyzed the polarization characteristics of the PePhC laser (supplementary figure S7), which showed a linear polarized output with degree of polarization (DOP) to be ≈ 70%. Linear polarization suggests finite deviation from perfect hexagonal PhC lattice symmetry and could result from the anisotropies due to imperfect nano-fabrication. Finally, to track the propagation of the emitted beams, we directed the laser output in the far field through a single slit to observe the expected clear diffraction pattern (Fig 3f). The intensity distribution after the slit can be well fitted by the $sinc^2$ function (white trace superimposed in Fig 3f).

To qualitatively assess the spectral range of the gain spectrum of the microcrystalline perovskite films, we studied the microlaser emission by varying the PhC dimensional parameters. As an example, Figure 4a shows the lasing spectrum from four different pitches of nanofabricated PhC substrates. The single mode lasing wavelengths range from 768.4 nm to 795.8 nm reflecting the Γ-point frequency shifts and the ability of the perovskite of fixed composition to support optical gain at least over an approximately 30 nm spectral window. As Fig. 4b shows, the threshold for each laser also varies, a result which is likely an aggregate of the net optical gain in the perovskite thin film and the Q-factor of the corresponding PhC. Lasing at λ = 788.1 nm (450 nm PhC pitch pattern) yielded the above mentioned lowest threshold; this wavelength also matches the minimum in the measured thin film extinction coefficient lending support for the spectral location for maximum optical gain (Fig. 2b). The total power conversion efficiency of the PePhC laser is estimated from measuring the output laser power versus absorbed pump laser power, yielding an external efficiency of 13.8% for the devices with the lowest threshold. Perhaps more important, from the slope of the laser performance above threshold, we measured directly a differential quantum efficiency 35.8% which compares well with established crystalline semiconductor diode lasers. We also observed how in the spontaneous emission regime, the PePhC devices with different PhC pitch

displayed different lineshapes as shown in supplementary Fig. S8, behavior which we speculate may partially reflect a spectral map of filtering effect from photonic crystal structure.[33]

Given the well-defined spatial output from the PePhC microlasers together with our custom fabrication process, a question arises of the scalability to compact multielement emitter arrays. Broadly, such pixelated arrays with individual addressability can be useful in applications such as high brightness displays, 3D modulated projection, etc. As a proof-of-concept we demonstrate here a 2D pixelated 4x4 PePhC microlaser array. The array was fabricated using methods described above (and in Supplement) by simply taking advantage of the PhC repeat patterns on the quartz substrate (here with 100 μm device-to-device pitch, while PhC pattern size is 75 μm × 75 μm). The laser elements in the array were switched on by programmed scanning of the optical pump laser by a MEMS mirror as shown schematically in Fig 5a. The voltage-controlled MEMS mirror scanning enabled controlled steering of the pump beam with 30 μm in radius to specific microlaser. (In this demonstration we used an available slow scanner with a dwell time ~10 ms on each laser pixel – much faster scanning for practical image projection use should be readily possible with faster optics). Figures 5b-g show photographic images from the PePhC array taken with an IR camera, beginning from PL emission out of 16 pixels (Fig. 5b) when pump power is below lasing threshold. In Figs. 5c-g, the pump beam is scanned across the array to generate specific pattern of the letters "X", "N", "L", "Z" and "C". For example, to generate letter "X", the scanning beam would dwell sequentially and periodically on pixel #1 → pixel #4 → pixel #6 → pixel #7 → pixel #10 → pixel #11 → pixel #13 → pixel #16.

Finally, we comment on a key important challenge for the rapidly expanding organometallic perovskite optoelectronic device research, namely the material stability and device lifetime. Active work is under way with solution-based perovskite solar cells concerning the role of the various traps and defects and their relationship to device performance and degradation.[36-38] Given the considerably higher levels of electronic excitation in perovskite light emitters (by two or three orders of magnitude), systematic studies lie ahead to determine the viability of the perovskite semiconductors as technologically competitive.

While beyond the scope of this paper, we mention briefly early results from our device lifetime studies of the new PePhC lasers - using the photoexcitation conditions described above (i.e. excluding the common practice in literature of deploying fsec pulses which do not provide a realistic point of reference). We have found in preliminary work that in these first PePhC lasers the output power decreased relatively quickly in time, to 50% after 6 mins. Heat induced effects can partially explain the power drop as we took no steps to heatsink or apply other types of heat management on this low thermal conductivity material.[39] Surprisingly and importantly, however, we have also found that this decrease in laser performance is substantially reversible (before pump energy density reaches excessive levels that induce visually obvious material damage). For example, the laser power recovered up to 90% of its initial value after a 20 mins "rest period" without photoexcitation in the ambient. This trend of recovery repeated itself during subsequent "lase-and-rest" episodes as summarized in Supplementary Fig. S9. Yet and under the same excitation conditions, the PL from the planar portion of our perovskite thin films was immune to this short-term decay phenomenon (Supplementary Fig. S10). With the caveat that any laser is sensitive to small variations in optical constants within the device, whether photoinduced or not, it is clear that much more detailed investigations await to dissect the roles of the various functional traps and those from material synthesis and device fabrication related contributions. Research on passivation and protection of the perovskite is under way in many laboratories in solar cell context and is relevant to our efforts as well.

In summary, we have developed a synergistic solution-based material synthesis and nanofabrication strategy to demonstrate low threshold practical perovskite-based photonic crystal band-edge laser. Importantly, spatially and spectrally coherent well-defined laser beams which are practically usable can now be produced from solution-based polycrystalline perovskite material, with the devices showing differential quantum efficiencies competitive with epitaxially grown single crystal semiconductor lasers. Our nanofabrication approach is scalable to larger area devices, such as the microlaser arrays demonstrated above. Likewise, our PhC based approach can be applied to other halide-perovskites using $PbCl_2$ or $PbBr_2$ as additional chemical precursors to reach shorter emission wavelengths across the visible.

Nanofabrication opportunities include other geometry such as a perovskite PhC laser with intentionally added "defect" [12-14] to enhance the photon confinement and light-matter interaction in a strong coupling regime. While only speculative at this point, electrical injection structures might also be integrable with the PhC configurations. Considerable additional work awaits to address device heat management, understand the microscopic process of the trap states to disable their non-radiative quenching, and explore the electronic excitations/states which underlie optical gain in the perovskites.

Methods

All the perovskite crystal growth and synthesis steps including spin-casting and thermal annealing were performed in N_2 atmosphere glove box with H_2O and O_2 level < 0.1 ppm and < 20 ppm, respectively. Optical characterization experiments were conducted using fresh perovskite films at room temperature and under ambient conditions (humidity ~ 21%) without any further protection. Absorbance spectra of the films were measured by Cary 500i UV-Vis-NIR Spectrometer and photoluminescence and lasing spectrum were obtained by Princeton Instrument ACTON Inspectrum spectrometer. The effective refractive index and extinction coefficient of the perovskite films were measured with variable angle spectroscopic ellipsometer (J. A. Woolam M-2000DI).

To fabricate the two dimensional photonic crystal nano-pillar array template, Poly(methyl methacrylate) (PMMA) electron beam resist was first spin-cast on top of a quartz substrate and baked. Electron beam writing (30 kV, 0.17 nA) was used to generate the designed PhC pattern (from numerical simulations). After the development of PMMA and the deposition of a 20 nm thick chromium layer as a hard mask, an inductively coupled plasma reactive ion etching (ICP-RIE) process was carried to complete fabrication of nano-pillar array with hexagonal lattice structure. To fabricate a perovskite thin film on planar or nanopatterned substrate, 50 μL of mixed precursor solution was spread onto the substrate, followed by 60

s spin-casting under 2000 rpm. At a specific time after start of spin-casting, 150 μL toluene was swiftly dripped vertically onto the center of the substrate. The as spin-cast film was then immediately transferred onto a 100 ºC hot plate for thermal annealing. Further details of the fabrication methods and process flow can be found under Supplementary Information.

References

1. Green, M. A., Ho-Baillie, A., & Snaith, H. J. The emergence of perovskite solar cells. *Nature Photon*. **8,** 506-514 (2014).
2. Xing, G. *et al.* Low-temperature solution-processed wavelength-tunable perovskites for lasing. *Nature Mater*. **13,** 476-480 (2014).
3. Zhang, Q., Ha, S. T., Liu, X., Sum, T. C., & Xiong, Q. Room-temperature near-infrared high-Q perovskite whispering-gallery planar nanolasers. *Nano Lett*. **14,** 5995-6001 (2014).
4. Liao, Q. *et al.* Perovskite microdisk microlasers self-assembled from solution. *Adv. Mater*. **27,** 3405–3410 (2015)
5. Zhu, H. *et al.* Lead halide perovskite nanowire lasers with low lasing thresholds and high quality factors. *Nature Mater*. **14,** 636-642 (2015).
6. Xing, J. *et al.* Vapor Phase Synthesis of Organometal Halide Perovskite Nanowires for Tunable Room-Temperature Nanolasers. *Nano Lett*. **15,** 4571-4577 (2015)
7. Dhanker, R. *et al.* Random lasing in organo-lead halide perovskite microcrystal networks. *Appl. Phys. Lett.* **105,** 151112 (2014).

8. Sutherland, B. R., Hoogland, S., Adachi, M. M., Wong, C. T., & Sargent, E. H. Conformal organohalide perovskites enable lasing on spherical resonators. *ACS Nano*. **8,** 10947-10952 (2014).
9. Deschler, F. *et al.* High photoluminescence efficiency and optically pumped lasing in solution-processed mixed halide perovskite semiconductors. *J. Phys. Chem. Lett*. **5,** 1421-1426 (2014).
10. Stranks, S. *et al*. Enhanced Amplified Spontaneous Emission in Perovskites using a Flexible Cholesteric Liquid Crystal Reflector. *Nano Lett*. **15,** 4935–4941 (2015).
11. Park, H. G. *et al*. Electrically driven single-cell photonic crystal laser. *Science*, **305,** 1444-1447 (2004).
12. Painter, O. *et al.* Two-dimensional photonic band-gap defect mode laser. *Science.* **284,** 1819-1821 (1999).
13. Akahane, Y., Asano, T., Song, B. S., & Noda, S. High-Q photonic nanocavity in a two-dimensional photonic crystal. *Nature.* **425,** 944-947 (2003).
14. Azzini, S. *et al*. Ultra-low threshold polariton lasing in photonic crystal cavities. *Appl. Phys. Lett.* **99,** 111106 (2001).
15. Ryu, H. Y., Kwon, S. H., Lee, Y. J., Lee, Y. H., & Kim, J. S. Very-low-threshold photonic band-edge lasers from free-standing triangular photonic crystal slabs. *Appl. Phys. Lett.* **80,** 3476-3478 (2002).
16. Kwon, S. H., Ryu, H. Y., Kim, G. H., Lee, Y. H., & Kim, S. B. Photonic bandedge lasers in two-dimensional square-lattice photonic crystal slabs. *Appl. Phys. Lett.* **83,** 3870-3872 (2003).
17. Ryu, H. Y., Notomi, M., & Lee, Y. H. Finite-difference time-domain investigation of band-edge resonant modes in finite-size two-dimensional photonic crystal slab. *Phys. Rev. B.* **68,** 045209 (2003).
18. Cho, C. O. *et al.* Photonic crystal band edge laser array with a holographically generated square-lattice pattern. *Appl. Phys. Lett.* **87,** 161102 (2005).
19. Dualeh, A. *et al.* Effect of annealing temperature on film morphology of organic–inorganic hybrid pervoskite solid state solar cells. *Adv. Funct. Mater.* **24,** 3250-3258 (2014).

20. Eperon, G. E., Burlakov, V. M., Docampo, P., Goriely, A., & Snaith, H. J. Morphological control for high performance, solution-processed planar heterojunction perovskite solar cells. *Adv. Funct. Mater.* **24,** 151-157 (2014).
21. Xiao, M. *et al.* A fast deposition-crystallization procedure for highly efficient lead iodide perovskite thin-film solar cells. *Angew. Chem.* **126,** 10056-10061 (2014).
22. Jeon, N. J. *et al.* Solvent engineering for high-performance inorganic–organic hybrid perovskite solar cells. *Nature Mater.* **13,** 897-903 (2014).
23. Liang, P. W. *et al.* Additive enhanced crystallization of solution-processed perovskite for highly efficient planar-heterojunction solar cells. *Adv. Mater.* **26,** 3748-3754 (2014).
24. Chen, C. W. *et al.* Efficient and Uniform Planar-Type Perovskite Solar Cells by Simple Sequential Vacuum Deposition. *Adv. Mater.* **26,** 6647-6652 (2014).
25. Liu, M., Johnston, M. B., & Snaith, H. J. Efficient planar heterojunction perovskite solar cells by vapour deposition. *Nature.* **501,** 395-398 (2013).
26. Malinkiewicz, O. *et al.* Perovskite solar cells employing organic charge-transport layers. *Nature Photon.* **8,** 128-132 (2014).
27. Zhang, W. *et al.* Ultrasmooth organic–inorganic perovskite thin-film formation and crystallization for efficient planar heterojunction solar cells. *Nat. Commun.* **6,** 6142 (2015).
28. Zhou, Y. *et al.* Room-temperature crystallization of hybrid-perovskite thin films via solvent–solvent extraction for high-performance solar cells. *J. Mater. Chem. A.* **3,** 8178-8184 (2015).
29. Wu, Y. *et al.* Retarding the crystallization of PbI_2 for highly reproducible planar-structured perovskite solar cells via sequential deposition. *Energy. Environ. Sci.* **7,** 2934-2938 (2014).
30. Im, J. H., Jang, I. H., Pellet, N., Grätzel, M., & Park, N. G. Growth of $CH_3NH_3PbI_3$ cuboids with controlled size for high-efficiency perovskite solar cells. *Nature Nanotech.* **9,** 927-932 (2014).
31. Xing, G. *et al.* Long-range balanced electron-and hole-transport lengths in organic-inorganic $CH_3NH_3PbI_3$. *Science.* **342,** 344-347 (2013).

32. Löper, P. *et al.* Complex Refractive Index Spectra of $CH_3NH_3PbI_3$ Perovskite Thin Films Determined by Spectroscopic Ellipsometry and Spectrophotometry. *J. Phys. Chem. Lett.* **6,** 66-71 (2014).
33. Pelton, Matthew. Modified spontaneous emission in nanophotonic structures. *Nature Photon.* **9,** 427-435 (2015).
34. Boroditsky, M. *et al.* Spontaneous emission extraction and Purcell enhancement from thin-film 2-D photonic crystals. *J. Lightw. Technol.* **17,** 2096 (1999).
35. Englund, D. *et al.* Controlling the spontaneous emission rate of single quantum dots in a two-dimensional photonic crystal. *Phys. Rev. Lett.* **95,** 013904 (2005).
36. Hoke, E. T. *et al.* Reversible photo-induced trap formation in mixed-halide hybrid perovskites for photovoltaics. *Chem. Sci.* **6,** 613-617 (2015).
37. Wu, X. *et al.* Trap States in Lead Iodide Perovskites. *J. Am. Chem. Soc.* **137,** 2089-2096 (2015).
38. Stranks, S. D. *et al.* Recombination Kinetics in Organic-Inorganic Perovskites: Excitons, Free Charge, and Subgap States. *Phys. Rev. Appl.* **2,** 034007 (2014).
39. Pisoni, A. *et al.* Ultra-Low Thermal Conductivity in Organic–Inorganic Hybrid Perovskite $CH_3NH_3PbI_3$. *J. Am. Chem.* Soc. **5,** 2488-2492 (2014).

Acknowledgements

The authors would like to thank for the financial support from the Department of Energy (Basic Energy Sciences) under grant: DE-FG02-07ER46387 and the Air Force Office of Scientific Research (AFOSR), and Quantum Metaphotonics and Metamaterails MURI (AFOSR Award No. FA9550-12-1-0488). The authors would also like to thank Financial support from NTU start-up grants M4080514 and M4081293, SPMS collaborative Research Award M4080536, Ministry of Education of Singapore.

Author contributions

S.C. designed the research, performed the experiments and analyzed the results. K.R. performed the film characterization for perovskite. J.L. and E.S. participated in analysis of the results. Y.L. and W.K.C. helped the perovskite thin film synthesis. N.M. and T.C.S. gave guidance on perovskite thin film fabrication. S.C., K.R, J.L., E.S., Y.L. and A.N. co-wrote the manuscript. A.N. contributed to all aspects of the work and led the research.

Additional information

The authors declare competing financial interests: details accompany the full-text HTML version of the paper at www.nature.com/naturenanotechnology. Supplementary information accompanies this paper at www.nature.com/naturenanotechnology. Reprints and permission information is available online at http://www.nature.com/reprints. Correspondence and requests for materials should be addressed to A.N.

Figure 1. Surface morphology of spin-cast closely packed perovskite films. The thin films were synthesized using DMSO as the host solvent and toluene "dripping time" of 37 s after the start of spin-casting. Thermal annealing at 100 ºC for 4 mins followed immediately after spin-casting. **a**, SEM image of film surface morphology of planar perovskite thin film. The scale bar is 1 μm. **b**, AFM scanning image from same film. The root mean square (RMS) surface roughness is 11.3 nm, indicative of an optically smooth surface. The scale bar is 500 nm. Photographs taken right after spin-casting and quick toluene dripping are shown in **c**, and after annealing in **d**, demonstrating optical transparency of the thin film. **f**, Cross-sectional SEM image; the scale bar is 200 nm. **e**, Absorbance (blue) and normalized PL (red) spectrum. The PL peak locates at 766.8 nm with FWHM of 50.1 nm. The relatively large FWHM linewidth suggests polydispersity in the size distribution of perovskite nanoscale grains.

Figure 2. Photonic crystal optical resonator design and characterization. a, Ellipsometry measurements yield the refractive index n (blue) and extinction coefficient k (red). The large refractive index (n = 2.6 ~ 2.7 in spectral region of interest) is consistent with the closely packed film; the lineshape of the extinction coefficient suggests a potential gain region around 760 ~ 820 nm. **b,** Plan view SEM image of 2D PhC showing the uniformity of the nanostructured pattern. The scale bar is 1 μm. Inset shows cross-sectional SEM image of perovskite film on 2D PhC pattern. The film deposits conformally with perovskite grains filling spaces between PhC nano-pillars with subsequent surface planarization. The scale bar is 400 nm. **c**, Calculation of photonic band structure of 2D hexagonal lattice PhC using PWE method with following parameters: a = 450 nm, r/a = 0.37, n_{quartz} = 1.50, $n_{perovskite}$ = 2.67. Inset identifies the principal directions in momentum space. **d**, Magnified view of photonic band structure of the circled (red dash line) in **c**.

Figure 3. Spatially and temporally coherent lasing from PePhC device with 450 nm pitch. a, Sharp threshold at input pulsed pump energy density of 68.5 ± 3.0 μJ/cm^2 is seen in emission, accompanied by collapse of the spectral linewidth from the spontaneous emission regime (Fig. 1g). Inset highlights the sharp threshold by same plot on logarithmic scale. **b**, Excitation dependence of the lasing spectrum above threshold. A single mode emission peak is seen at 788.1 nm with a 0.24 nm linewidth. Inset shows photographic images taken by an adjacent IR camera, perpendicular to the sample plane with excitation below (left) and above (right) threshold, respectively. The PhC pattern size is 75 μm × 75 μm. **c**, time-resolved emission kinetics comparing the spontaneous and lasing regimes (P_{pump} = 1.1 P_{th}), with measured decay time constants of 5.44 ± 0.06 ns (blue dots) and 112.8 ± 9.8 ps (red dots), respectively. **d**,**e**, Details of the far field beam patterns from laser devices showing two spatially coherent transverse modes (θ_x and θ_y are the horizontal and vertical divergence angles). The transverse mode in **d** is dominated in most cases, reflecting the selection of a single Γ-point eigenmode in the lasing process. **f**, Single slit diffraction pattern imaged after propagating the PePhC output laser beam though a narrow rectangular aperture. The transmitted intensity distribution is well-fitted by function $I(\theta) = I_0 \,\mathrm{sinc}^2\left(\pi d/\lambda \sin(\theta)\right)$, where d is the slit width, λ is the wavelength and θ is the diffraction angle (shown as the white trace). The fitted slit width 96.1 μm matches well with directly measured slit width 93.4 μm.

Figure 4. PePhC lasing with different pitch photonic crystal patterns. a, Lasing output from PhC with pitch range of 430 ~ 460 nm. Single mode lasing is seen at 768.4 nm, 777.3 nm, 788.1 nm and 795.8 nm. **b**, Threshold (blue) and efficiency (red) results at each lasing wavelength. The 450 nm pitch pattern

achieves the lowest threshold 65.5 μJ/cm^2 and highest output/input power conversion efficiency of 13.8%. The thresholds for 430 nm, 440 nm, 460 nm pitch patterns are 141.3 μJ/cm^2, 79.7 μJ/cm^2, 82.3 μJ/cm^2, with corresponding efficiency 5.2%, 11.6%, 8.2%, respectively.

Figure 5. Programmable, spatially patterned lasing from a 2D pixelated PePhC laser array. a, Schematic configuration for the demonstration experiment. The MEMS scanning mirror is voltage-controlled by a Labview program to steer the pump laser beam to different positions on sample, focusing down to 30 μm in radius by focal lens. Emitted beam from each PePhC microlaser (perpendicular to device plane) is collected after long pass filter which blocks any residue pump excitation. The lower right corner figure shows the 4×4 device array configuration and pixel numbering. Each PePhC device has dimension as 75 μm × 75 μm with 25 μm gap between each two adjacent devices. **b**, Spatially integrated photographic image when the 16 pixels are targeted up sequentially in the spontaneous emission regime. **c-g**, Different spatial laser beam patterns generated from the array using pre-programmed scanning protocol, here showing the letters "X", "N", "L", "Z", "C". For example, to generate letter "C", the periodical pump laser scan sequence was: pixel #2 → pixel #3 → pixel #8 → pixel #12 → pixel #14 → pixel #15.

Figure 1

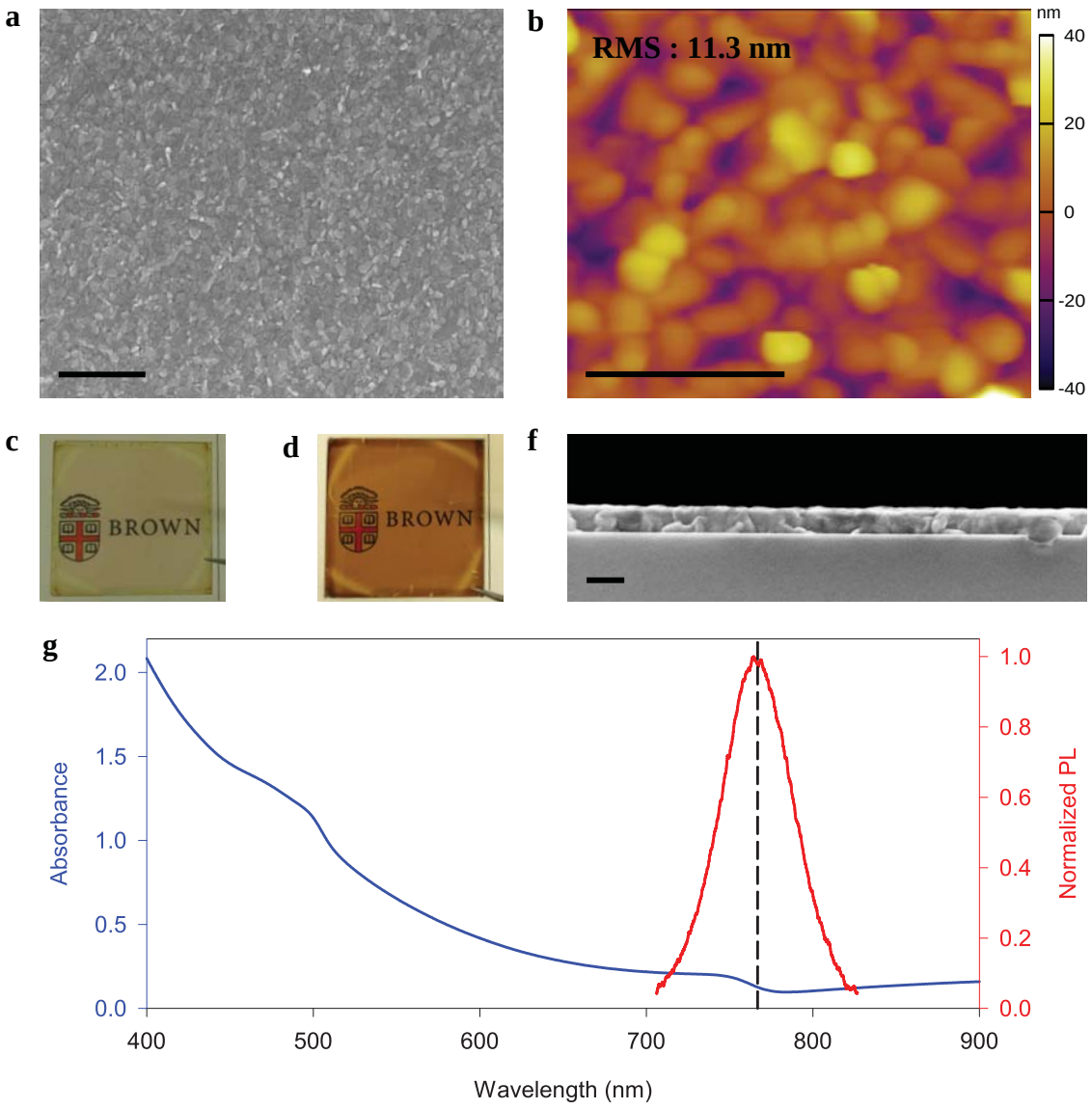
a
b
RMS : 11.3 nm
nm
40
20
0
-20
-40
c
BROWN
d
BROWN
f
g
Absorbance
Normalized PL
Wavelength (nm)
2.0
1.5
1.0
0.5
0.0
1.0
0.8
0.6
0.4
0.2
0.0
400
500
600
700
800
900

Figure 2

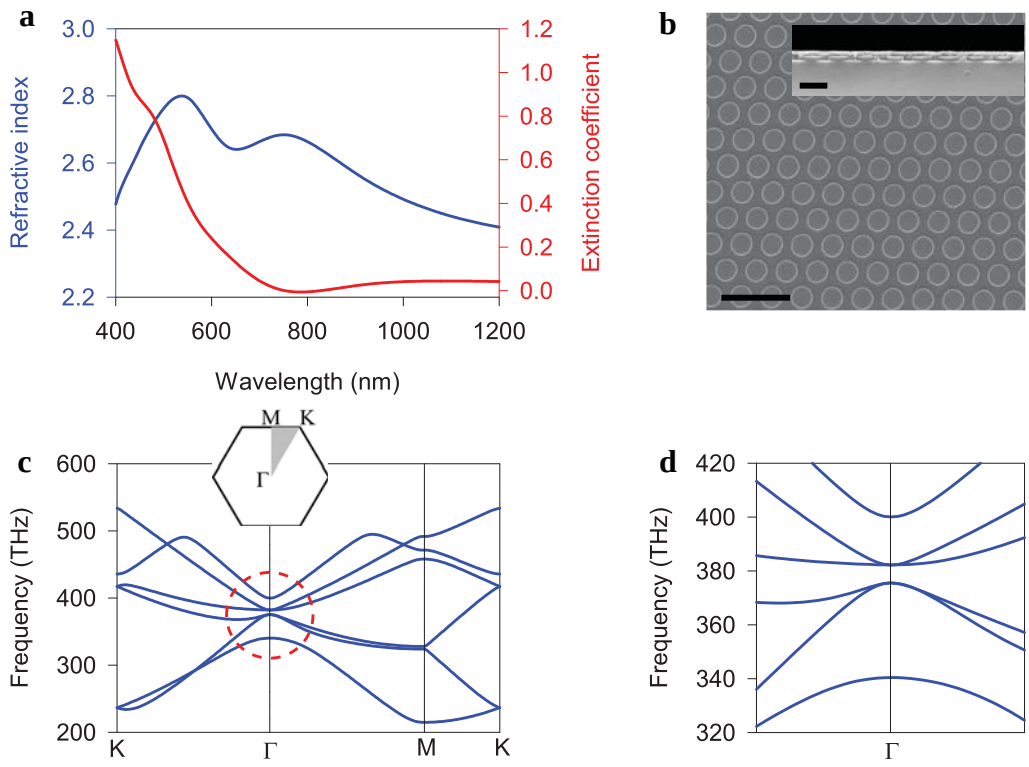
a
Refractive index
Extinction coefficient
Wavelength (nm)
3.0
2.8
2.6
2.4
2.2
1.2
1.0
0.8
0.6
0.4
0.2
0.0
400
600
800
1000
1200
b
c
Frequency (THz)
600
500
400
300
200
M K
Γ
K
Γ
M
K
d
Frequency (THz)
420
400
380
360
340
320
Γ

Figure 3

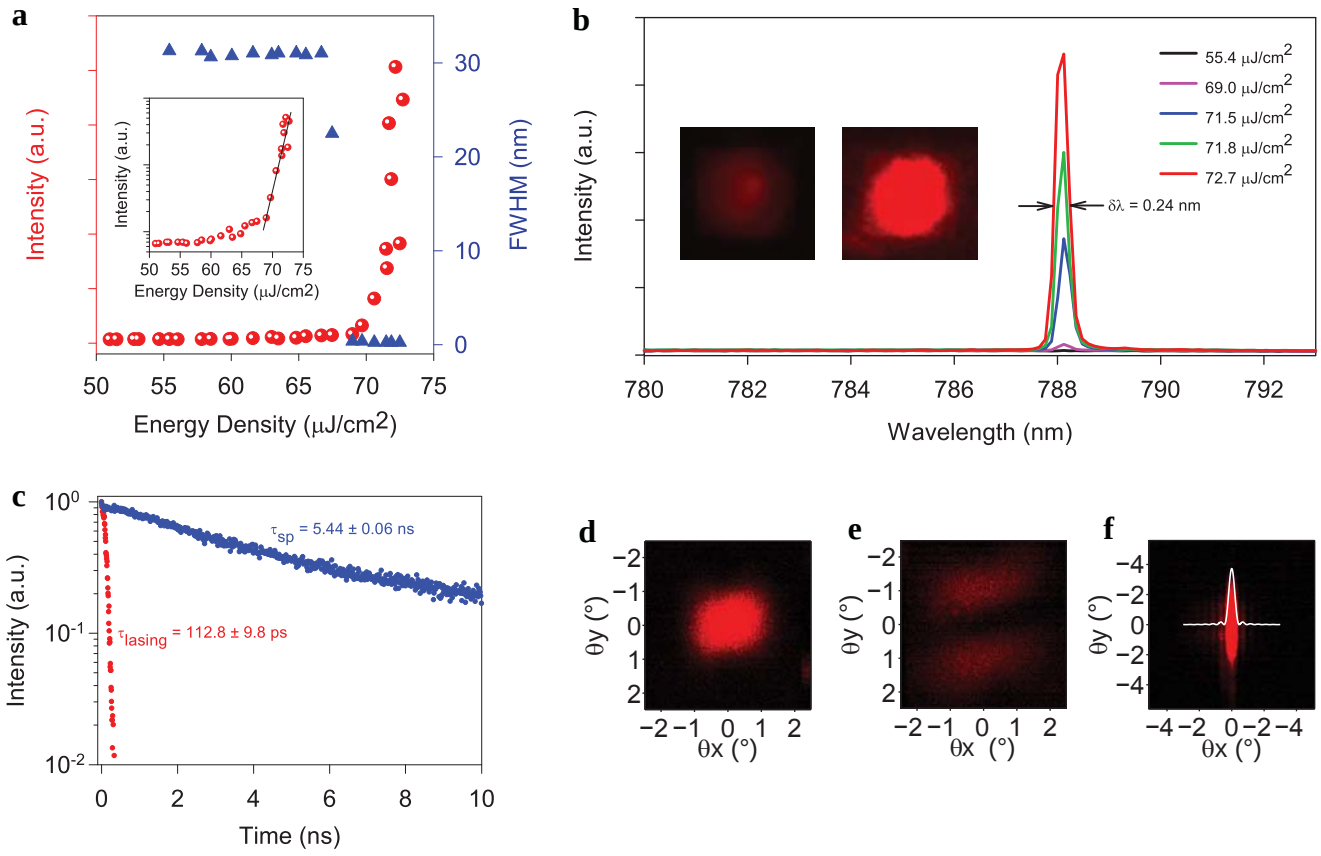
a
Intensity (a.u.)
FWHM (nm)
Energy Density (μJ/cm2)
Intensity (a.u.)
Energy Density (μJ/cm2)
b
Intensity (a.u.)
55.4 μJ/cm2
69.0 μJ/cm2
71.5 μJ/cm2
71.8 μJ/cm2
72.7 μJ/cm2
δλ = 0.24 nm
Wavelength (nm)
c
Intensity (a.u.)
τsp = 5.44 ± 0.06 ns
τlasing = 112.8 ± 9.8 ps
Time (ns)
d
e
f
θy (°)
θx (°)

Figure 4

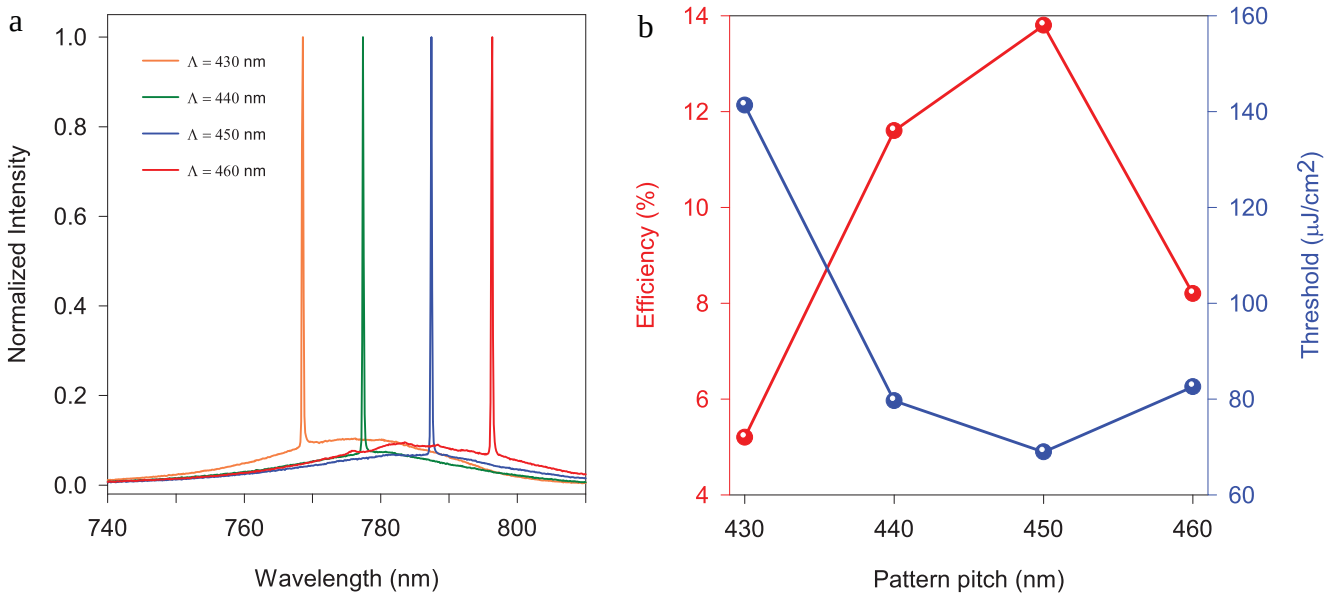
a
Normalized Intensity
1.0
0.8
0.6
0.4
0.2
0.0
Λ = 430 nm
Λ = 440 nm
Λ = 450 nm
Λ = 460 nm
740
760
780
800
Wavelength (nm)
b
Efficiency (%)
14
12
10
8
6
4
Threshold (μJ/cm2)
160
140
120
100
80
60
430
440
450
460
Pattern pitch (nm)

Figure 5

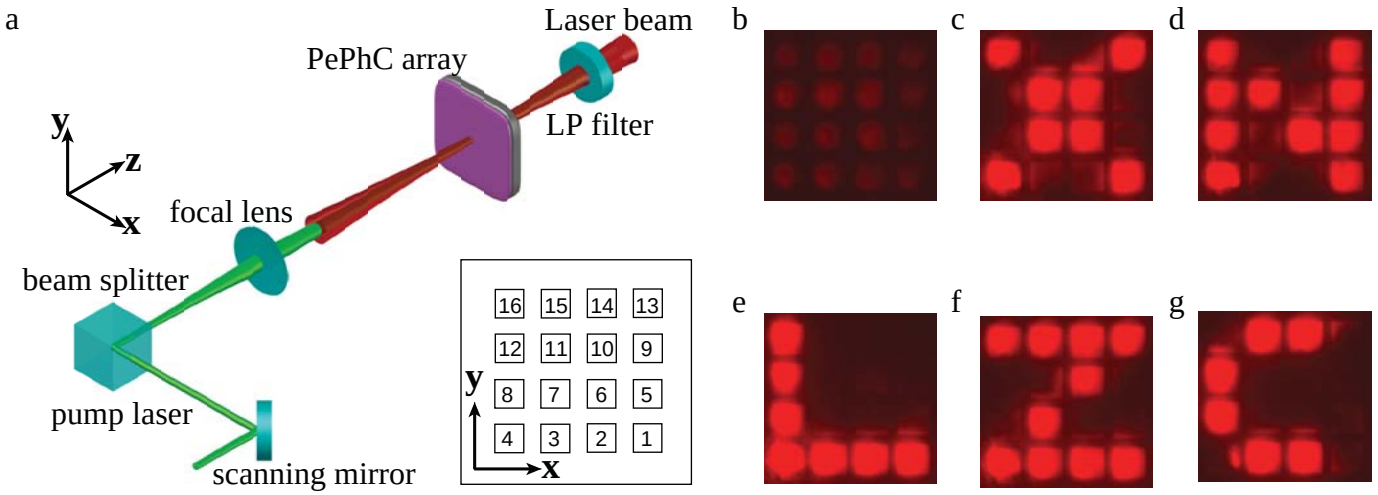
a
Laser beam
PePhC array
LP filter
y
z
x
focal lens
beam splitter
pump laser
scanning mirror
16 15 14 13
12 11 10 9
8 7 6 5
4 3 2 1
y
x
b
c
d
e
f
g